JGR Atmospheres

RESEARCH ARTICLE
10.1029/2018JD029908

Shading by Trees and Fractional Snow Cover Control the Subcanopy Radiation Budget

Johanna Malle[1,2], Nick Rutter[1], Giulia Mazzotti[2,3], and Tobias Jonas[2]

[1]Department of Geography and Environmental Sciences, Northumbria University, Newcastle upon Tyne, UK, [2]WSL Institute for Snow and Avalanche Research SLF, Davos Dorf, Switzerland, [3]Laboratory of Hydraulics, Hydrology and Glaciology VAW, ETH, Zurich, Switzerland

Key Points:
- Radiation measurements were taken concurrently with downlooking hemispherical imagery to determine the spatial extent of shaded/sunlit snow
- Shading by trees and fractional snow cover were shown to exert key controls on the subcanopy radiation budget
- Subcanopy radiation measurements revealed a linear relationship between outgoing shortwave radiation and the view fraction of sunlit snow

Correspondence to:
J. Malle,
johanna.malle@northumbria.ac.uk

Citation:
Malle, J., Rutter, N., Mazzotti, G., & Jonas, T. (2019). Shading by trees and fractional snow cover control the subcanopy radiation budget. *Journal of Geophysical Research: Atmospheres*, *124*, 3195–3207. https://doi.org/10.1029/2018JD029908

Received 31 OCT 2018
Accepted 26 FEB 2019
Accepted article online 4 MAR 2019
Published online 21 MAR 2019

The copyright line for this article was changed on 22 APR 2019 after original online publication.

Abstract Radiative processes are substantially altered by the presence of forest canopies, further affecting snow energetics during wintertime. In situ measurements of subcanopy radiation can help improve process-scale understanding of these complex interactions, which are needed to further constrain and improve land surface models. In this study, a custom-made cable car was used to measure incoming and outgoing, shortwave and longwave radiation below an evergreen forest stand. Hemispherical photographs taken concurrently from the cable car measured view fractions of shaded snow, sunlit snow, and bare ground. With this setup it was possible to quantify diurnal and seasonal radiation patterns together with their potential drivers at high spatiotemporal resolution. Measurements were performed between January and May 2018, along a 48-m transect in a discontinuous needleleaf forest in the Swiss Alps. Analysis of diurnal radiation patterns revealed a strong linear relationship ($R = 0.94$) between outgoing shortwave radiation and sunlit snow-view fraction, highlighting shading as the main control on the subcanopy shortwave radiation budget. Measurements of outgoing longwave radiation were strongly controlled by the snow cover extent, with locations of diminished snow cover showing an increase in outgoing longwave radiation of up to 60 W/m^2. The subcanopy radiation budget was shown to be dominated by shortwave radiation when surrounding canopy structure and the position of the sun allowed for direct insolation of the forest floor, but longwave radiation was the dominating component in the absence of direct insolation.

1. Introduction

The presence of trees exerts a principal control on snow dynamics in forested environments (Musselman & Pomeroy, 2017; Roth & Nolin, 2017), further affecting energy exchanges between the land surface and the atmosphere (Bonan et al., 1992; Loranty et al., 2014) and impacting hydrological regimes (Lundquist et al., 2013) as well as the Earth's carbon balance of snow-dominated regions (Pulliainen et al., 2017; Sturm et al., 2001). Given that across the Northern Hemisphere 20% of seasonally snow-covered areas reside within forested environments (Rutter et al., 2009), process-scale understanding of interactions between snow, vegetation, and climate as well as their representation in local, regional, and global land surface schemes is of major importance, which, to date, remains a particular challenge (Loranty et al., 2014; Yuan et al., 2017).

On the local scale, forested environments create microclimates that alter snowpack dynamics with increased spatial and temporal variability (Ellis et al., 2011; Lundquist et al., 2013). One of the main drivers of this forest-induced heterogeneity is the fact that the subcanopy energy budget and consequently the snow cover energy budget are strongly controlled by radiation (Ellis et al., 2011; Link & Marks, 1999; Sicart et al., 2004). Compared to open areas, the presence of a forest canopy attenuates shortwave radiation and allows for enhancement of longwave radiation (thermal emissions) by absorption of shortwave and reemittance as longwave energy (e.g., Sicart et al., 2004), further affecting timing, intensity, and duration of snow melt (Male & Granger, 1981). Accurate prediction of meltwater runoff from snow-dominated forested watersheds as well as of energy fluxes between the land surface and the atmosphere therefore requires reliable estimates of radiative transfer processes through vegetation canopies, including net radiation on the forest floor (Lawler & Link, 2011; Seyednasrollah & Kumar, 2014).

Net shortwave radiation is controlled by incoming shortwave radiation and also strongly influenced by surface albedo, which modulates the absorption of incoming shortwave radiation. Generally, the low albedo of trees has the potential to mask high snow albedo (Bonan, 2008), which decreases the overall reflectivity of

the land surface (Betts & Ball, 1997), further having a warming effect on climate (Abe et al., 2017). However, over complex surfaces, the ratio between upwelling and downwelling radiation, referred to as effective albedo, is not only a function of the albedo of individual surface elements. Over a forest, for instance, the upwelling shortwave radiation is strongly modulated by canopy shading of the ground (Webster & Jonas, 2018). The concept of effective albedo has been used in studies investigating its dynamics over rough snow and ice surfaces (Lhermitte et al., 2014; Pirazzini, 2004), over mountainous terrain (Weihs et al., 2001) as well as in urban settings (Sailor & Fan, 2002). Surface reflectance properties are hence combined with multiple reflections and local shading phenomena. Overall, effective surface albedo of forested, snow-covered areas is controlled by tree species (Kuusinen et al., 2014), forest structure (Bright et al., 2018), and seasonality (Kuusinen et al., 2012). Solar angle and the interlinked canopy shading (Webster & Jonas, 2018) as well as intercepted snow (Bartlett & Verseghy, 2015) further alter effective surface albedo of forested environments. Subcanopy effective albedo is an important indicator of the energy absorbed by the ground and the canopy that can be applied to validate simulations of radiation transfer through the canopy, for example, performing intercomparison studies between one-layer and multilayer canopy models (e.g., Gouttevin et al., 2015).

One method to obtain information of the Earth's surface radiation budget is to use remotely sensed satellite data. While broadband satellite products are useful for radiation retrieval over large spatial extents (Schaaf et al., 2002; Wang et al., 2009), the resolution is too coarse to capture the small-scale variability in snow energetics of forested environments since the most commonly used Moderate-resolution Imaging Spectroradiometer (MODIS) data products are available at a 500-m gridded spatial resolution (Campagnolo et al., 2016; Román et al., 2009), and even 30-m Land Remote Sensing Satellite (LANDSAT) albedo retrievals (e.g., Wang et al., 2016) do not adequately capture the heterogeneity of gaps and edges within a forest stand. Fine-scale satellite remote sensing products (i.e., WorldView-4 by DigitalGlobe) are emerging but are not capable of capturing subcanopy radiative regimes, making in situ radiation measurements still indispensable when aiming to improve process-scale understanding of radiative transfer through a canopy. However, the use of a single stationary radiometer is not adequate to represent the heterogeneity of a forest stand (Link et al., 2004); previous studies have therefore used radiometer arrays of various extents (Pomeroy et al., 2008; Seyednasrollah & Kumar, 2014; Webster et al., 2016a), which are associated with high costs, and are not capable of capturing outgoing radiation. Moving rail systems have been used as an alternative approach to capture spatiotemporal radiation patterns below a forest stand over lengths ranging from 10 to 60 m to investigate the effects of foliage clumping (Law et al., 2001), seasonal trends of diurnal energy balance in boreal aspen forests (Blanken et al., 2001) as well as transpiration dynamics (Vrugt et al., 2002). Such a moving rail system has also been deployed in a snow-dominated environment (Stähli et al., 2009; Webster et al., 2016b), but the rail system only covered a relatively small distance (10 m) in a fairly dense forest. However, moving rail systems have the potential to capture radiative transfer processes in snow-dominated, forested environments, providing high spatiotemporal subcanopy radiation data. These high quality in situ observations are needed to constrain, validate, and improve radiation parametrization of current land surface model schemes for forested regions (Qu & Hall, 2014; Wild et al., 2001).

This paper presents a novel data set of distributed subcanopy radiation measurements in a discontinuous evergreen needleleaf forest stand in the Swiss Alps. A moving net radiometer was used to measure incoming and outgoing shortwave and longwave radiation, alongside a camera to quantify the hemispherical view fractions of shaded snow, sunlit snow, bare ground (all downlooking), as well as sky and canopy (uplooking). Analysis focuses on both diurnal and seasonal radiation patterns below an evergreen forest stand with four main objectives, which each quantify (1) the influence of shading on both outgoing shortwave radiation as well as subcanopy effective albedo, (2) the effect of solar angle and forest structure on the subcanopy radiation budget, (3) the effect of fractional snow cover on outgoing longwave radiation, and (4) the relative importance of shortwave and longwave radiation on the subcanopy all-wave radiation budget.

2. Methods

2.1. Field Site

Figure 1a shows the study site located close to Davos Laret, Switzerland, (46°50′40″N, 9°52′29″E, 1,530 m.a.s.l) in a discontinuous forest stand with the predominant species being Norwegian spruce. An 8-mm steel cable was secured between two trees, 51 m apart, ranging from an open, discontinuous forest at the west

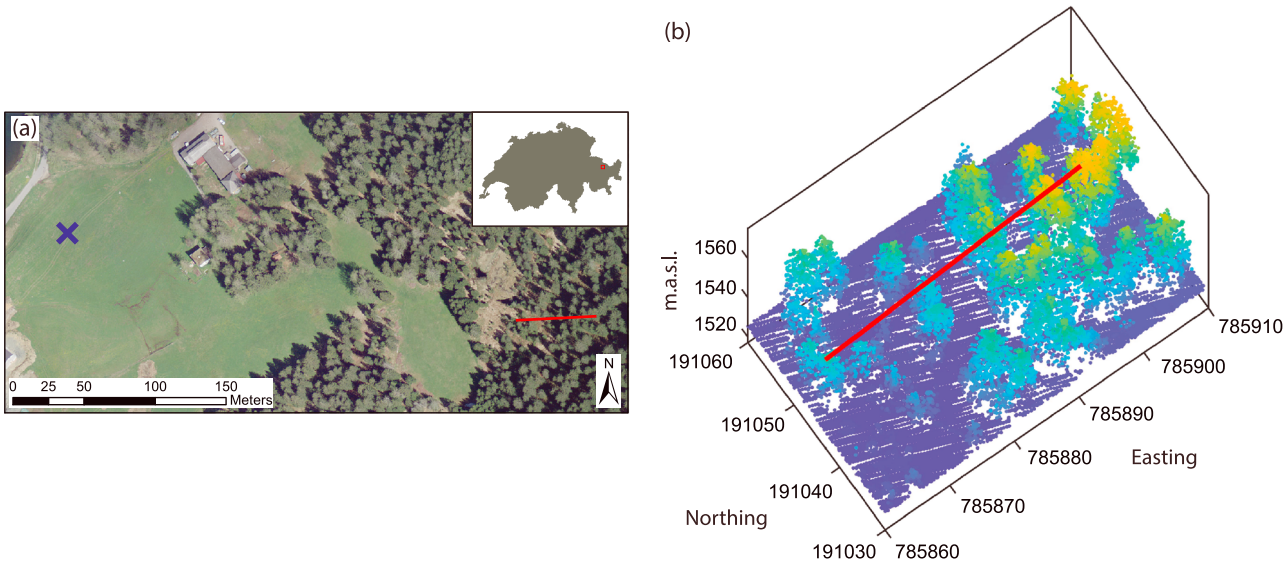

Figure 1. (a) Layout of the field site in Laret, Switzerland, where the red line indicates the cable car transect and the blue cross shows the reference meteorological station. (b) A 3-D LiDAR plot visualizing the forest stand surrounding the cable car transect.

end to a more dense forest at the east end (Figure 1b). The cable remained level to an accuracy of ±1° across the 51 m, while the height above ground varied between 1 and 3 m depending on local surface topography and snow height. A meteorological reference station, located at an open area 300 m to the west of the installed cable, provided a continuous data set of atmospheric boundary conditions (incoming longwave and shortwave radiation, outgoing shortwave radiation, air temperature, relative humidity, snow height, wind speed, wind direction, and precipitation) at 30-min resolution for the time span between December 2017 and May 2018.

2.2. Cable Car System

A custom-made cable car (Figure 2) controlled the position of measurements along the cable. The cable car included uplooking and downlooking shortwave and longwave radiation sensors (Kipp and Zonen CMP3 pyranometers and CGR3 pyrgeometers) as well as a downlooking Sony Alpha NEX6 16.1MP camera with a Yasuhara Madoka f/4 7.3 mm 180° fisheye lens. Furthermore, an inclinometer (Kelag KAS901-51A) recorded the tilt of the system in x and y direction to an accuracy of 0.01°. The cable car moved at a constant speed of 0.07 m/s, while the radiation sensors, connected to a Campell Scientific CR1000 data logger, measured at 1-s intervals. In accordance with the response time (18 s) of the radiation sensors, data were

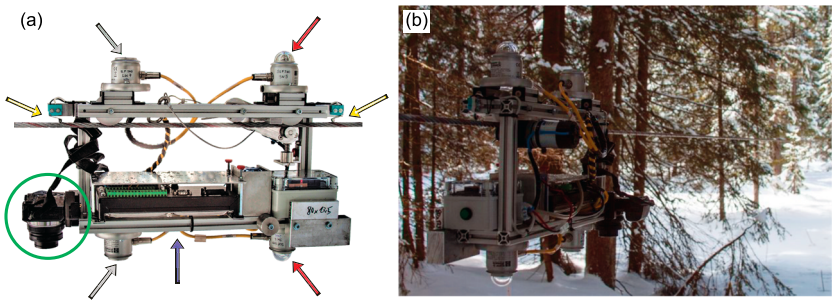

Figure 2. Cable car system attached to the steel cable. (a) Red arrows point at uplooking and downlooking CMP3 shortwave radiation sensors, gray arrows at uplooking and downlooking CGR3 longwave radiation sensors, yellow arrows at the switches on either end of the cable car, and the purple arrow indicates the location of the inclinometer. The hemispherical camera (in this case mounted to achieve down-looking hemispherical imagery) is highlighted with a green circle. (b) Field picture of cable car system.

aggregated into 42 sections along the cable, providing an independent measurement every ~1.1 m. Movement was controlled by a motor (Micro motors E192.12.67) and powered by a 5,200-mAh Li-Ion battery and switches on each end of the cable car allowed for automatic reversal in direction upon reaching the end of the cable. The effective measurement length between the two cable ends was 48 m.

2.3. Meteorological Conditions

Figures 3a and 3b show above canopy meteorological conditions from the open site reference station and the 17 different days between January and May 2018 when transect runs of radiation measurements were made using the cable car system. On two selected clear-sky days (red arrows in Figure 3a), one at the start (18.4.2018) and one in the middle (25.4.2018) of melt season, continuous radiation measurements were performed throughout the entire day from before sunrise to after sunset. Both days had very similar meteorological conditions (see Figures 3c and 3d), with the main difference being a reduction in snow cover extent. Measurements collected during these two clear-sky days were used to analyze diurnal radiation patterns of incoming, outgoing, and net shortwave as well as longwave radiation, while the data from all campaigns are used to investigate seasonal trends.

2.4. Calculation of Hemispherical View Fractions

Ground surface conditions were obtained by analyzing downlooking hemispherical photographs. The downlooking Sony NEX6 camera (Figure 2) was set to trigger every 5 s (Sony Time-lapse App, V3.40), resulting in 110–120 images along each 48-m transit. Of those images, 42 were selected that were best collocated with the respective spatial aggregation units of the radiation measurement. Each selected downlooking hemispherical photograph was analyzed to obtain the following hemispherical view fractions: Ground-view fraction (VF_{Ground}), sunlit snow-view fraction (VF_{Sun}), and shaded snow-view fraction (VF_{Shade}). VF_{Ground} refers to all snow-free surfaces, including both bare ground and canopy elements, whereas VF_{Sun} and VF_{Shade} are separating snow-covered surfaces into sunlit and shaded areas. To arrive at the different view fractions, a two-stage manual thresholding was used: (1) pixels were classified into either snow (white) or ground/stems (black) to determine VF_{Ground}, and (2) pixels classified as snow in stage 1 were further separated into sunlit snow (white pixel) from shaded snow (black pixel) to determine VF_{Sun}. VF_{Shade} was then calculated as a residual using the following:

$$VF_{Shade} = 1 - VF_{Ground} - VF_{Sun} \quad (1)$$

Solar radiation of shaded areas predominantly consists of the diffuse component, further enhancing the presence of blue light, whereas bare ground and canopy elements mostly consist of red and green light. While all three RGB (Red Green Blue) bands were used to select a threshold to distinguish between sunlit and shaded snow pixels, only the blue band was used when categorizing each pixel into snow or ground. By only using the blue band, contrast between snow and bare ground/stems is improved and cast shadows of surrounding trees are ignored (Webster & Jonas, 2018; Wolter et al., 2012). This approach has been suggested by previous studies for separation of canopy and sky pixels in traditional uplooking hemispherical photographs (Leblanc et al., 2005; Nobis & Hunziker, 2005; Reid & Essery, 2013; Zhang et al., 2005).

Once the threshold was selected, each hemispherical image was discretized into 10 concentric analysis rings, and the ratio between black and white pixels within each analysis ring was calculated and further weighted by the sine of the elevation angle to determine VF_{Ground}, VF_{Sun}, and VF_{Shade}, following the approach applied by Essery et al. (2008) on upward looking hemispherical images. When the snow cover fraction is 100%, VF_{Ground} reflects the fraction of trunks in the 180° view field of a hemispherical photograph, which gives the baseline reference for snow cover extent calculations. VF_{Ground} was only calculated once per day to account for melt out of snow, while VF_{Sun} and VF_{Shade} had to be determined for each transit due to the changing solar angles. Figure 4 shows an example downlooking hemispherical photograph as well as the resulting categorized image indicating the extents of VF_{Ground}, VF_{Sun}, and VF_{Shade}.

During an overcast day with uniform light conditions, the Sony Alpha NEX6 camera was attached at the top of the cable car system in order to obtain sky-view fraction (VF_{Sky}) to quantify forest density along the observed transect. The images were analyzed using the same methods as for VF_{Ground}, VF_{Sun}, and VF_{Shade}. Figure 5 shows the resulting VF_{Sky} along the transect, which was constant throughout the winter season.

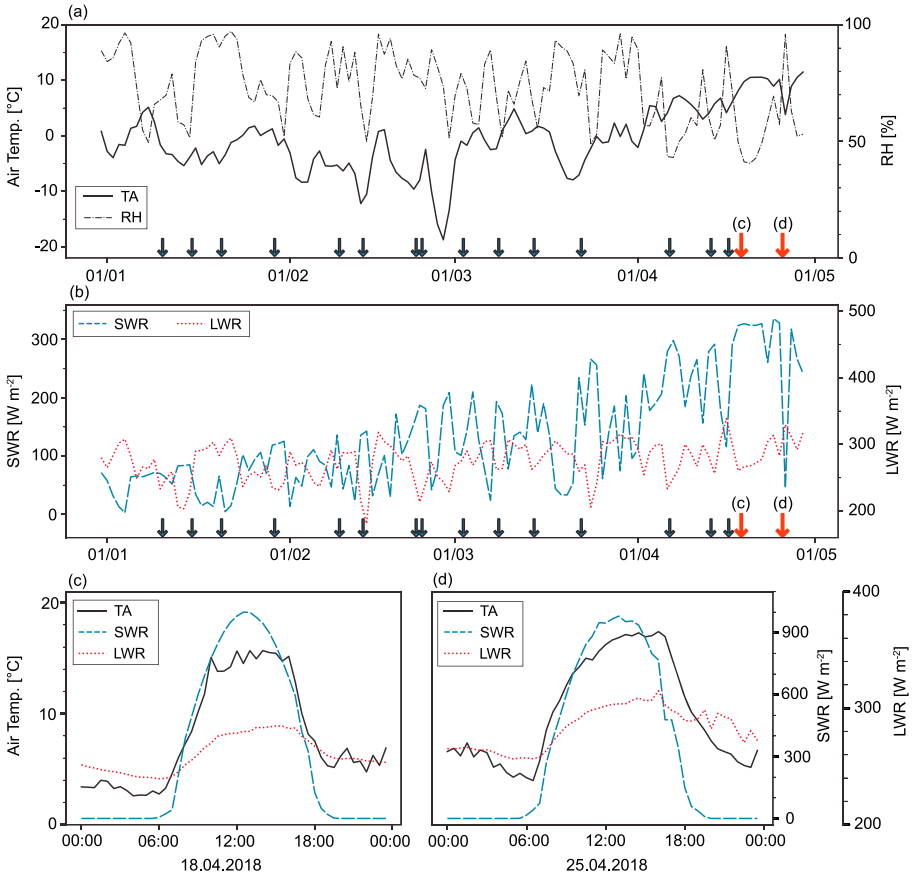

Figure 3. Meteorological conditions at the reference open site. Daily averages from January until May 2018 are shown for (a) air temperature and relative humidity as well as for (b) incoming shortwave (SWR) and longwave radiation (LWR). Arrows at the bottom indicate days when cable car measurements were performed. Larger red arrows indicate the 2 days of continuous radiation measurements (18.4.2018, 25.4.2018) for which the meteorological conditions are visualized in (c) and (d).

VF_{Sky} ranged from 0.10 at the dense, east end of the transect to 0.46 at the west end where the forest cover was discontinuous. Figure 5 further indicates how VF_{Ground} ranged from 0.01 to 0.32 during full snow cover conditions on 18 April—indicating the baseline trunk view fraction along the transect—and how it was increased to ranging from 0.16 to 0.93 on 25 April due to partial melt out.

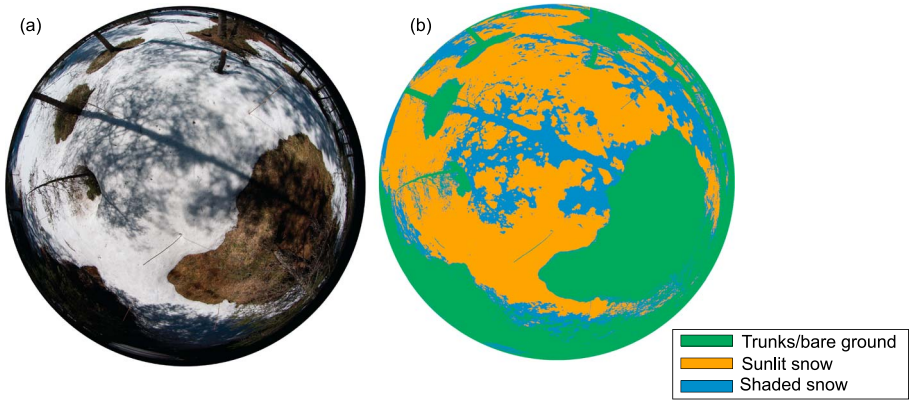

Figure 4. (a) Exemplary downlooking hemispherical photograph used to investigate ground conditions.(b) Analyzed image, distinguishing between bare ground/stems (green), sunlit snow (orange), and shaded snow (blue).

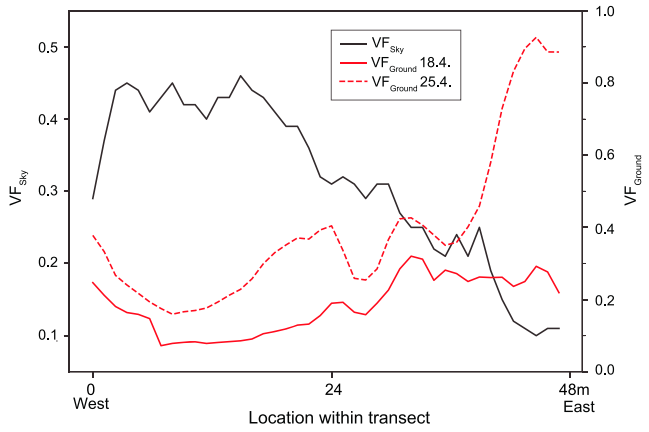

Figure 5. Cross-sectional view of the cable car transect indicating sky-view fraction (VF_{Sky}) and ground-view fraction (VF_{Ground}) along the 48-m transect. VF_{Sky} remained constant between the 2 days.

3. Results

3.1. Subcanopy Shortwave Radiation Patterns: Diurnal Analysis

Figure 6 contrasts the diurnal patterns of 18 April and 25 April 2018 of shortwave radiation (SWR) fluxes and sunlit snow-view fraction. Meteorological conditions were almost identical between the 2 days (see Figure 2); forest structure was constant, and the solar declination angle was only changing minimally; therefore, the incoming SWR patterns between 18 and 25 April were nearly the same (see Figures 6a and 6b). High spatial and temporal data resolution allowed detailed measurement of small changes in meteorological conditions (e.g., cirrus cloud moving through in the afternoon of 25 April) as well as interactions between forest structure and the changing daytime solar position. For instance, sections with high/low insolation moved over the day to the east, as the sun moved to the west, leading to diagonal patterns visible in all panels of Figure 6.

Outgoing subcanopy SWR (Figures 6c and 6d) was influenced by patterns of incoming SWR, but fine-scale imprints of the forest structure were not present in the data due to a higher fraction of diffuse radiation in reflected SWR. The maximum outgoing SWR on 18 April was 403 W/m^2, which was lower by 24% at 305 W/m^2 on 25 April. Differences in outgoing SWR between the two observed days were coincident with both an increase in VF_{Ground} (smaller fractional snow cover, shallower snow pack, and more trunks visible) and a decrease in the albedo of the remaining snow surface (snow age and litter). Some differences were notable at the eastern end of the transect, where most of the melt out had happened.

Patterns of VF_{Sun} (Figures 6e and 6f) resembled the outgoing SWR patterns for both days, with high sunlit snow-view fractions occurring at locations with high outgoing SWR, while locations where outgoing SWR was low were mostly shaded. Similarities between diurnal patterns of outgoing SWR and VF_{Sun} demonstrated the strong control shading had on subcanopy radiation. This is further illustrated by Figure 7, which contrasts outgoing SWR and VF_{Sun} for all data points collected during full snow cover conditions (18 April 2018), further implying a strong positive relationship (correlation coefficient $R = 0.94$) between outgoing SWR and VF_{Sun}. Figure 7 also shows how during low zenith angles, which occurred around local solar noon, a large variability was observed in both outgoing SWR and VF_{Sun}. During low zenith angles, the western part of the transect where canopy closure was sparse showed high values in VF_{Sun}, while the east part was too dense for sun rays to penetrate through the canopy and therefore corresponded to low VF_{Sun}. During high zenith angles, shadows were predominant throughout the entire transect, resulting in a smaller range in both outgoing SWR and VF_{Sun}.

Effective albedo patterns are shown in Figures 6g and 6h. Measured effective albedo >1 occurred predominantly at transitions from continuous ($VF_{Sky} < 0.2$) to discontinuous forest, where trees sheltered the uplooking pyranometer from incoming SWR while the snow surface below was still sunlit. At these locations, effective albedo values of up to 2 were measured on 18 April and up to 1.5 on 25 April. Contrasting effective albedo values of 18 and 25 April further show the substantially lower effective albedo on 25 April at the eastern end of the transect where most of the snow had already melted.

3.2. Subcanopy Longwave Radiation Patterns: Diurnal Analysis

Figure 8 illustrates longwave radiation (LWR) along the transect for 18 April and 25 April, respectively. In contrast to SWR-related data shown in Figure 6, spatiotemporal patterns of LWR include vertical and diagonal features, the former being related to stationary effects such as LWR irradiance from snow-free ground or canopy elements, the latter reflecting temporary heating from absorption of direct SWR.

On both days subcanopy incoming LWR was particularly high at locations with low VF_{Sky} (Figures 8a and 8b). Increases in below canopy incoming longwave radiation were especially pronounced in the afternoons, once diurnal increases in above canopy shortwave radiation had heated the forest canopy, which due to internal heat storage of the canopy remained effective until after sunset. On 25 April, emittance of LWR

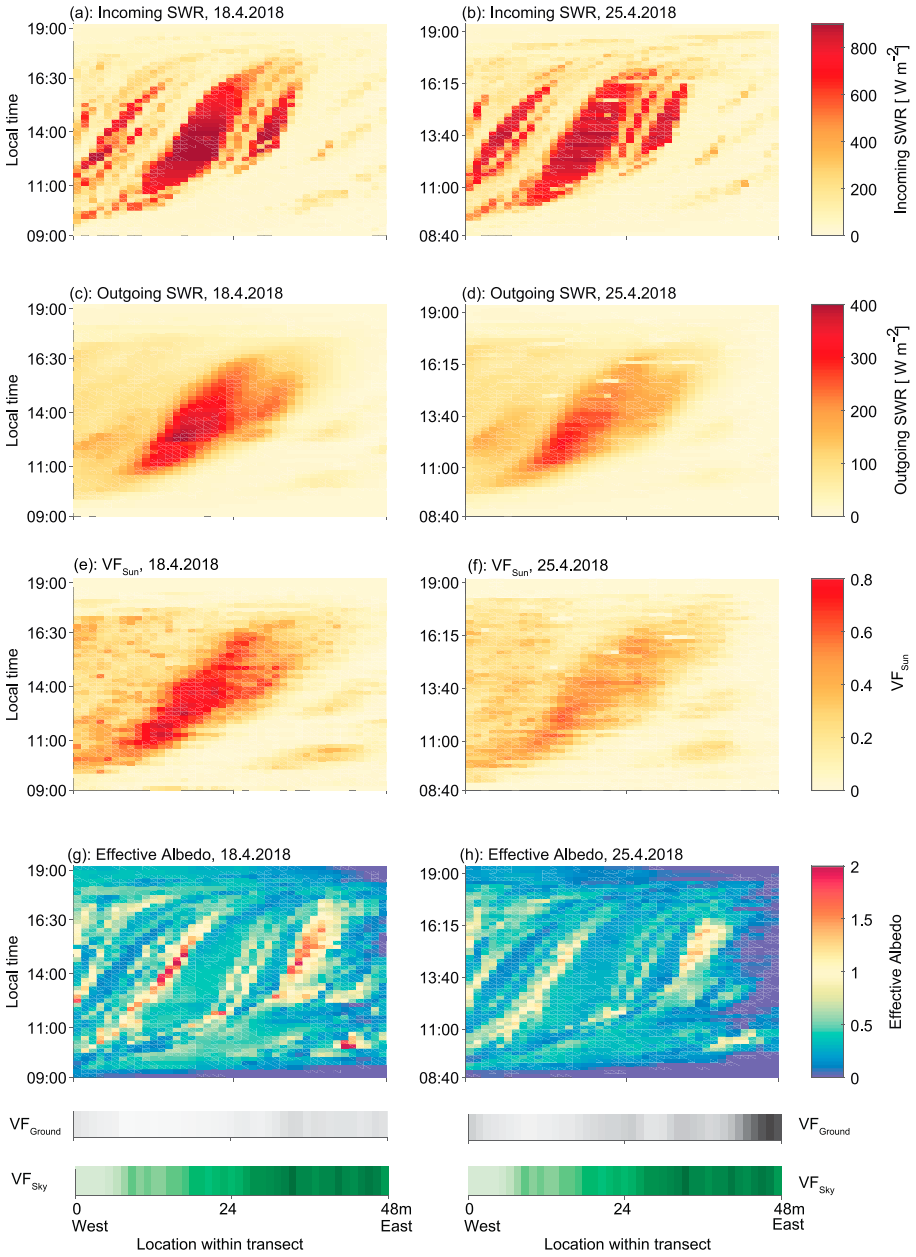

Figure 6. Shortwave radiation (SWR) patterns for 18 April (full snow cover) and 25 April 2018 (partial snow cover). (a, b) Visualize incoming SWR, (c, d) outgoing SWR, (e, f) sunlit snow-view fraction (VF_{Sun}), and (g, h) effective albedo for the respective days. The color bars below show VF_{Ground} (white = 0, black = 1) and VF_{Sky} (white = 1, dark green = 0) along the transect for each day. Note that VF_{Ground} and VF_{Sky} are quantified in Figure 5.

from the canopy was especially enhanced due to warmer midday air temperatures (see Figures 3c and 3d), leading to incoming longwave radiation of up to 403 W/m^2.

On 18 April, still featuring continuous subcanopy snow cover, daytime outgoing LWR throughout the day was constantly between 320 and 338 W/m^2. While snow temperature never exceeds 0 °C, which corresponds to a maximum LWR emittance of 309 W/m^2, the surface temperatures of both litter on the snow surface and of trunks and other canopy elements in the view field of the sensor were able to increase outgoing LWR by up to 30 W/m^2. However, on 25 April, a further increase in outgoing LWR was evident. While 25 April was warmer than 18 April, the difference in VF_{Ground} (Figure 5) substantially altered outgoing longwave radiation, particularly to the east of the transect. Similar to incoming LWR, outgoing

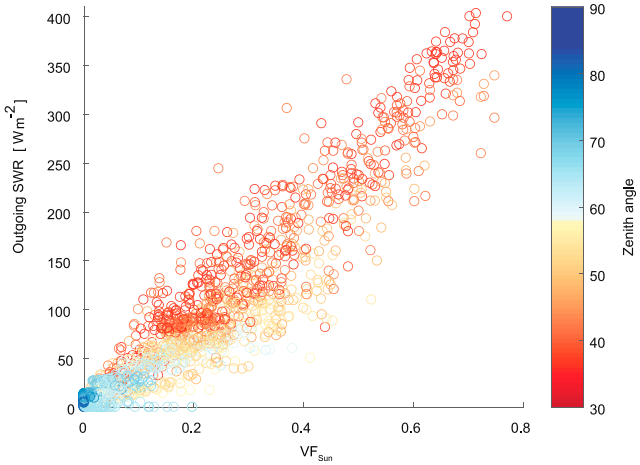

Figure 7. Sunlit snow-view fraction (VF_{Sun}) versus outgoing shortwave radiation (SWR) during a sunny day and full snow cover conditions (18 April 2018). Each data point represents a single measurement along the transits on 18 April 2018.

LWR above snow-free areas was especially pronounced in the afternoon after several hours of high solar insolation of the ground.

The difference between incoming and outgoing LWR resulted in a surface net longwave radiation as visualized in Figures 8e and 8f. On 18 April, the net LWR ranged from net negative downward fluxes of up to 25 W/m^2 at the more discontinuous western part of the transect and to a net positive downward flux of up to 50 W/m^2 at the denser eastern part of the transect. Locations of the highest downward flux on 18 April and the associated increase in energy available for snow melt aligned well with those areas where snow disappeared between 18 and 25 April (see Figure 5). As the melt season progressed, increased upwelling LWR over snow-free areas resulted in an attenuation of the net positive downward flux, which occasionally even led to net negative downward fluxes (Figure 8f).

3.3. Subcanopy Net All-Wave Radiation Patterns: Diurnal Analysis

Combining the four components of the radiation budget resulted in net all-wave radiation, which is visualized in Figures 9a and 9b for 18 and 25 April 2018, respectively. At first sight it appeared that shortwave radiation dominated the all-wave radiation, but this was only the case when the position of the sun and the overlying canopy structure allowed direct insolation of the ground surface. In forests, direct insolation of the ground may be restricted to relatively short periods during clear-sky days, while positive net longwave radiation may occur over extended periods and across all 24 hr of a day. In the absence of direct insolation, net LWR patterns dominate the net all-wave radiation. Negative net all-wave radiation occurred for 5% of all data points on 18 April and only for 1% of data points on 25 April. These data points tend to also have effective albedo values above 1, further emphasizing the importance of accurately representing subcanopy effective albedo.

3.4. Seasonal Analysis of Shortwave Radiation

Extending the analysis to all measurements performed between January and May 2018 (Figure 3) allowed investigation of seasonal effects on the relationship between incoming and outgoing SWR. For the purpose of this seasonal analysis, measurements of each cable car transit were spatially averaged. Snow conditions for each measurement day were further classified into full, partial, or no snow cover. As seen in Figure 10, reflected and incoming SWR were constrained by the zenith angle of the sun's position, while the effective albedo decreased with snow cover fraction. Further variation in effective albedo can be explained by snow age, litter, and the fractions of sunlit and shaded snow. Given the spatial averaging of the data presented, effective albedo values above 1 were not recorded. Note that in this analysis, only data acquired during clear-sky/partially cloudy conditions (sky emissivity <0.8) were included. During cloudy conditions, SWR is mostly diffuse and ground-shading patterns are less distinct, leading to smaller variations in both incoming and outgoing SWR due to a changing solar angle.

4. Discussion

In situ measurements of wintertime subcanopy radiation in an evergreen needleleaf forest showed high spatiotemporal heterogeneity. Data presented build upon previous studies (e.g., Link & Marks, 1999; Sicart et al., 2004; Webster et al., 2016b) which monitored spatiotemporal variability of subcanopy irradiance to illustrate the strong control solar angle and vegetation structure have on the radiation budget of a forested environment, which further governs melt patterns (Ellis et al., 2010; Sicart et al., 2004). However, the novelty of this data set is the additional spatiotemporal quantification of the view fractions of shaded and sunlit snow, as well as snow cover extent. These were shown to exert strong influence on the outgoing radiation components below a forest stand. The importance of canopy shading for radiative processes in snow-dominated environments has been highlighted by previous studies, as Betts and Ball (1997) observed a lowering of snow albedo due to the effect of canopy shading in boreal forests and Webster and Jonas (2018) showed shading to be of significant importance for effective albedo above a needleleaf evergreen forest. Data presented in this study, however, combined subcanopy shaded/sunlit-snow view fractions and

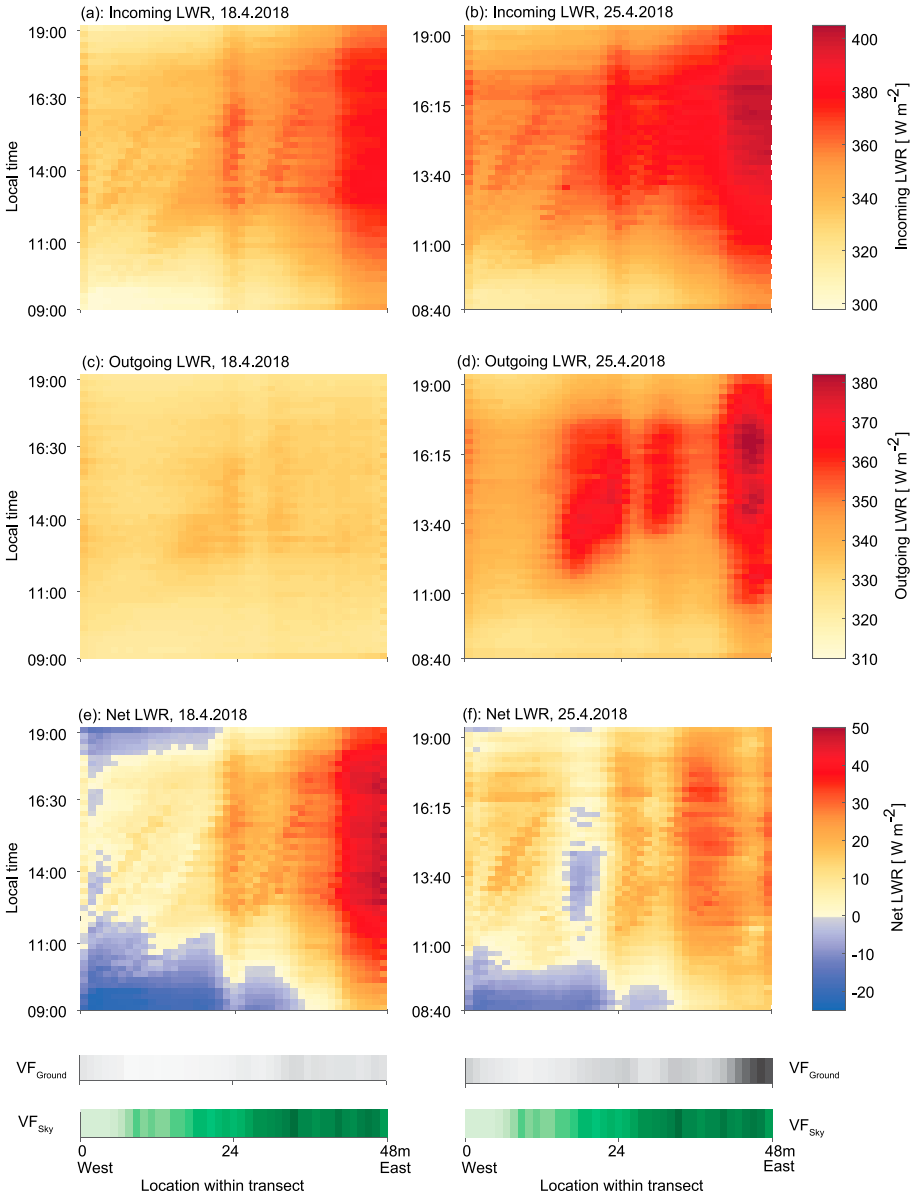

Figure 8. Longwave radiation (LWR) LWR patterns for 18 April (full snow cover) and 25 April 2018 (partial snow cover). (a, b) Visualize incoming LWR, (c, d) outgoing LWR, and (e, f) net LWR flux ($LWR_{incoming} - LWR_{outgoing}$) for the respective days. The color bars below show VF_{Ground} (white = 0, black = 1) and VF_{Sky} (white = 1, dark green = 0) along the transect for each day. Note that VF_{Ground} and VF_{Sky} are quantified in Figure 5.

radiation measurements, allowing the importance of shading to be quantified on a previously unavailable, spatially and temporally distributed scale.

Solar angle and forest structure controlled the relative position of the sun to the trees and hence the resulting size and shape of canopy shadows on the snow surface (smallest at local solar noon, largest during high zenith angles), which further govern diurnal patterns of shaded/sunlit snow-view fractions. The similarity in diurnal patterns and the resulting strong linear relationship between outgoing shortwave radiation and sunlit snow-view fraction underline the importance of shading, further suggesting that it is a key control of the subcanopy radiation budget.

Energy fluxes have a high seasonal variability which were also represented by highly variable effective albedos during different land surface conditions: no snow, partial snow, and full snow cover extent. Measured

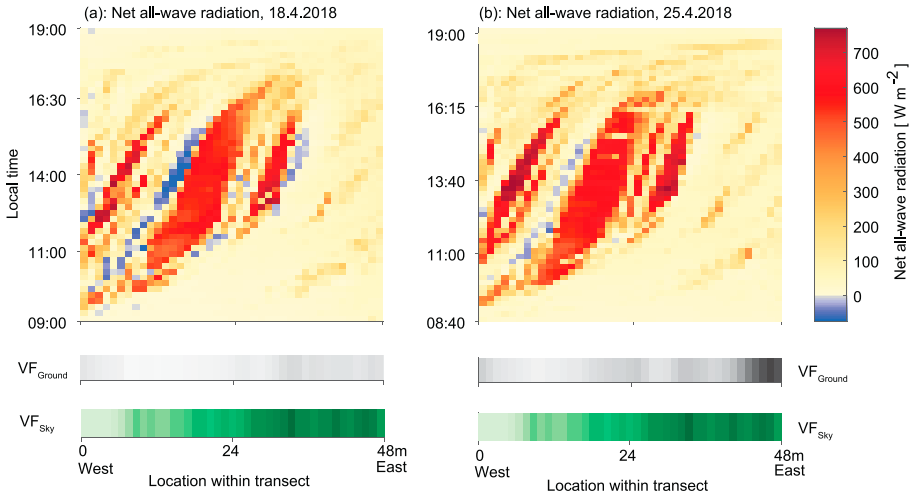

Figure 9. Net radiation for (a) 18 April and (b) 25 April 2018. The color bars below show VF_{Ground} (white = 0, black = 1) and VF_{Sky} (white = 1, dark green = 0) along the transect for each day, as quantified in Figure 5.

effective albedo was shown to decrease through the winter season. While this study only investigated the effect of partial snow cover, littering from canopy debris (e.g., Winkler et al., 2010) as well as snow aging due to increased surface grain size (Wiscombe & Warren, 1980) and thinning of the snow cover (allowing absorbance by ground) further affected seasonal albedo development. The highest effective albedo values were measured midwinter, when solar irradiance was generally low. Under these conditions, the effect of albedo on climatic processes tends to be smaller than during springtime when high insolation increases its importance (Kuusinen et al., 2012). Consequently, accurately quantifying partial snow cover when aiming to calculate subcanopy outgoing shortwave radiation and the resulting effective albedo is of major importance for land surface modeling.

In addition to affecting shortwave fluxes, the presence of canopies also altered longwave radiation fluxes. Forest structure determined the relative importance of longwave radiation, as proximity to denser forest surroundings coincided with stronger longwave radiation enhancement, which is in line with findings of previous studies (e.g., Klos & Link, 2018; Pomeroy et al., 2009). Sicart et al. (2004) demonstrated that during low solar irradiance, in combination with full snow cover (high effective albedo) and low atmospheric emissivity, canopy-induced attenuation of shortwave radiation is offset by longwave enhancement, further increasing net all-wave radiation and impacting snow melt patterns. Results obtained from the cable car system affirm this result. During full snow cover conditions, measured net positive downward LWR fluxes during springtime were of similar magnitude (50–60 W/m^2) to previous studies (Musselman & Pomeroy, 2017; Webster et al., 2016b). Magnitudes of peak subcanopy incoming longwave radiation further increased throughout the melt period due to amplified air and canopy temperatures, which supports results by Webster et al. (2016b). The cable car system further allowed quantification of snow cover extent over a spatially distributed extent and related it to outgoing longwave radiation. During partial snow cover conditions, outgoing longwave radiation was dependent on snow cover extent, as areas of bare ground increased the outgoing longwave radiation by up to 60 W/m^2, increasing the potential for negative net longwave radiation. The relationship between solar angle and timing of heat storage and release by both the canopy and bare ground during fractional snow cover conditions is an important aspect that should be considered when modeling subcanopy longwave radiation (e.g., Pomeroy et al., 2009; Webster et al., 2016b).

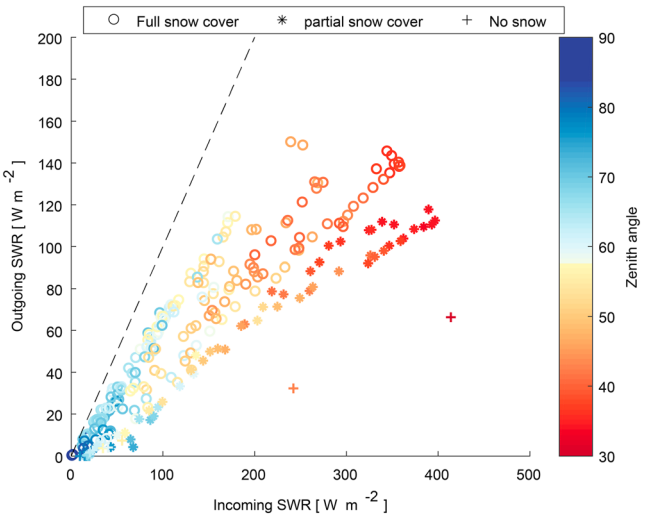

Figure 10. Seasonal analysis of reflected versus incoming SWR. Each data point represents an averaged transect run, colors assign zenith angle, and symbol indicates full snow/partial snow cover or no snow conditions. The dashed line is the 1:1 line, indicating an effective albedo of 1.

Furthermore, explicitly solving for shaded surfaces below a forest canopy as well as separating between direct and diffuse radiation can considerably upgrade land surface modeling. Musselman et al. (2015) found that by conceptualizing canopy gaps as circular cylinders and explicitly resolving shading in a ray tracing model environment, the spatially heterogeneous diurnal radiation of a forest gap could be simulated more reliably. The potential for inclusion of shading in large-scale modeling is increasing, as recent land surface model developments have started to incorporate the 3-D canopy structures (Yuan et al., 2014) as well modifying the commonly used two-stream approximation to account for horizontally heterogeneous canopy structures (Yuan et al., 2017). Accounting for the effects of shading and fractional snow cover on the subcanopy radiation budget should be a priority for further land-surface model enhancement across forested environments.

5. Conclusions

A custom-made cable car system enabled high-resolution uplooking and downlooking shortwave and longwave radiation measurements with simultaneous hemispherical photographs of the ground conditions. This allowed quantification of the influence of shading and fractional snow cover on the subcanopy radiation budget. Spatiotemporal analysis of data collected during a clear-sky day revealed a strong linear relationship between outgoing shortwave radiation and sunlit snow-view fraction ($R = 0.94$), highlighting shading as a key control of the subcanopy shortwave radiation budget. Fractional snow cover was shown to be of particular importance for outgoing longwave radiation, as snow cover extent was reflected by an increase in outgoing longwave radiation of up to 60 W/m^2 over areas where snow had melted. Net all-wave radiation was dominated by shortwave radiation whenever direct insolation of the forest floor occurred; however, at times and locations where canopy structure inhibited direct insolation (which is the case during most of the day), longwave radiation was controlling the subcanopy radiation budget.

Acknowledgments
The authors thank Elena Stautzenbach, Luca Iacolettig, and Sarah Barr for assistance in the field. Data presented in this study are available from the WSL data repository Envidat at their website (www.envidat.ch/dataset/forest-radiation-data). We thank Dr. Keith Musselman and one anonymous reviewer for their insightful comments and suggestions which helped improve the quality of the manuscript.

References

Abe, M., Takata, K., Kawamiya, M., & Watanabe, S. (2017). Vegetation masking effect on future warming and snow albedo feedback in a boreal forest region of northern Eurasia according to MIROC-ESM. *Journal of Geophysical Research: Atmospheres*, *122*, 9245–9261. https://doi.org/10.1002/2017JD026957

Bartlett, P. A., & Verseghy, D. L. (2015). Modified treatment of intercepted snow improves the simulated forest albedo in the Canadian Land Surface Scheme. *Hydrological Processes*, *29*(14), 3208–3226. https://doi.org/10.1002/hyp.10431

Betts, A. K., & Ball, J. H. (1997). Albedo over the boreal forest. *Journal of Geophysical Research*, *102*(D24), 28,901–28,909. https://doi.org/10.1029/96JD03876

Blanken, P. D., Black, T. A., Neumann, H. H., De Hartog, G., Yang, P. C., Nesic, Z., & Lee, X. (2001). The seasonal water and energy exchange above and within a boreal aspen forest. *Journal of Hydrology*, *245*(1–4), 118–136. https://doi.org/10.1016/S0022-1694(01)00343-2

Bonan, G. B. (2008). Forests and climate change: Forcings, feedbacks, and the climate benefits of forests. *Science*, *320*(5882), 1444–1449. https://doi.org/10.1126/science.1155121

Bonan, G. B., David, P., & Thompson, S. L. (1992). Effects of boreal forest vegetation on global climate. *Nature*, *359*(6397), 716–718. https://doi.org/10.1038/359716a0

Bright, R. M., Eisner, S., Lund, M. T., Majasalmi, T., Myhre, G., & Astrup, R. (2018). Inferring surface albedo prediction error linked to forest structure at high latitudes. *Journal of Geophysical Research: Atmospheres*, *123*, 4910–4925. https://doi.org/10.1029/2018JD028293

Campagnolo, M. L., Sun, Q., Liu, Y., Schaaf, C., Wang, Z., & Román, M. O. (2016). Estimating the effective spatial resolution of the operational BRDF, albedo, and nadir reflectance products from MODIS and VIIRS. *Remote Sensing of Environment*, *175*, 52–64. https://doi.org/10.1016/j.rse.2015.12.033

Ellis, C. R., Pomeroy, J. W., Brown, T., & MacDonald, J. (2010). Simulation of snow accumulation and melt in needleleaf forest environments. *Hydrology and Earth System Sciences*, *14*(6), 925–940. https://doi.org/10.5194/hess-14-925-2010

Ellis, C. R., Pomeroy, J. W., Essery, R. L. H. H., & Link, T. E. (2011). Effects of needleleaf forest cover on radiation and snowmelt dynamics in the Canadian Rocky Mountains. *Canadian Journal of Forest Research*, *41*(3), 608–620. https://doi.org/10.1139/X10-227

Essery, R., Pomeroy, J., Ellis, C., & Link, T. (2008). Modelling longwave radiation to snow beneath forest canopies using hemispherical photography or linear regression. *Hydrological Processes*, *22*(15), 2788–2800. https://doi.org/10.1002/hyp.6930

Gouttevin, I., Lehning, M., Jonas, T., Gustafsson, D., & Mölder, M. (2015). A two-layer canopy model with thermal inertia for an improved snowpack energy balance below needleleaf forest (model SNOWPACK, version 3.2.1, revision 741). *Geoscientific Model Development*, *8*(8), 2379–2398. https://doi.org/10.5194/gmd-8-2379-2015

Klos, P. Z., & Link, T. E. (2018). Quantifying shortwave and longwave radiation inputs to headwater streams under differing canopy structures. *Forest Ecology and Management*, *407*(July 2017), 116–124. https://doi.org/10.1016/j.foreco.2017.10.046

Kuusinen, N., Kolari, P., Levula, J., Porcar-Castell, A., Stenberg, P., & Berninger, F. (2012). Seasonal variation in boreal pine forest albedo and effects of canopy snow on forest reflectance. *Agricultural and Forest Meteorology*, *164*, 53–60. https://doi.org/10.1016/j.agrformet.2012.05.009

Kuusinen, N., Lukeš, P., Stenberg, P., Levula, J., Nikinmaa, E., & Berninger, F. (2014). Measured and modelled albedos in Finnish boreal forest stands of different species, structure and understory. *Ecological Modelling*, *284*, 10–18. https://doi.org/10.1016/j.ecolmodel.2014.04.007

Law, B. E., van Tuyl, S., Cescatti, A., & Baldocchi, D. D. (2001). Estimation of leaf area index in open-canopy ponderosa pine forests at different successional stages and management regimes in Oregon. *Agricultural and Forest Meteorology*, *108*(1), 1–14. https://doi.org/10.1016/S0168-1923(01)00226-X

Lawler, R. R., & Link, T. E. (2011). Quantification of incoming all-wave radiation in discontinuous forest canopies with application to snowmelt prediction. *Hydrological Processes*, *25*(21), 3322–3331. https://doi.org/10.1002/hyp.8150

Leblanc, S. G., Chen, J. M., Fernandes, R., Deering, D. W., & Conley, A. (2005). Methodology comparison for canopy structure parameters extraction from digital hemispherical photography in boreal forests. *Agricultural and Forest Meteorology*, *129*(3–4), 187–207. https://doi.org/10.1016/j.agrformet.2004.09.006

Lhermitte, S., Abermann, J., & Kinnard, C. (2014). Albedo over rough snow and ice surfaces. *The Cryosphere*, *8*(3), 1069–1086. https://doi.org/10.5194/tc-8-1069-2014

Link, T. E., & Marks, D. (1999). Point simulation of seasonal snow cover dynamics beneath boreal forest canopies. *Journal of Geophysical Research*, *104*(D22), 27,841–27,857. https://doi.org/10.1029/1998JD200121

Link, T. E., Marks, D., & Hardy, J. P. (2004). A deterministic method to characterize canopy radiative transfer properties. *Hydrological Processes*, *18*(18), 3583–3594. https://doi.org/10.1002/hyp.5793

Loranty, M. M., Berner, L. T., Goetz, S. J., Jin, Y., & Randerson, J. T. (2014). Vegetation controls on northern high latitude snow-albedo feedback: Observations and CMIP5 model simulations. *Global Change Biology*, *20*(2), 594–606. https://doi.org/10.1111/gcb.12391

Lundquist, J. D., Dickerson-Lange, S. E., Lutz, J. A., & Cristea, N. C. (2013). Lower forest density enhances snow retention in regions with warmer winters: A global framework developed from plot-scale observations and modeling. *Water Resources Research*, *49*, 6356–6370. https://doi.org/10.1002/wrcr.20504

Male, D. H., & Granger, R. J. (1981). Snow surface energy exchange. *Water Resources Research*, *17*(3), 609–627. https://doi.org/10.1029/WR017i003p00609

Musselman, K. N., & Pomeroy, J. W. (2017). Estimation of needleleaf canopy and trunk temperatures and longwave contribution to melting snow. *Journal of Hydrometeorology*, *18*(2), 555–572. https://doi.org/10.1175/JHM-D-16-0111.1

Musselman, K. N., Pomeroy, J. W., & Link, T. E. (2015). Variability in shortwave irradiance caused by forest gaps: Measurements, modelling, and implications for snow energetics. *Agricultural and Forest Meteorology*, *207*, 69–82. https://doi.org/10.1016/j.agrformet.2015.03.014

Nobis, M., & Hunziker, U. (2005). Automatic thresholding for hemispherical canopy-photographs based on edge detection. *Agricultural and Forest Meteorology*, *128*(3–4), 243–250. https://doi.org/10.1016/j.agrformet.2004.10.002

Pirazzini, R. (2004). Surface albedo measurements over Antarctic sites in summer. *Journal of Geophysical Research*, *109*, D20118. https://doi.org/10.1029/2004JD004617

Pomeroy, J. W., Gray, D. M., & Marsh, P. (2008). Studies on snow redistribution by wind and forest, snow-covered area depletion, and frozen soil infiltration in Northern and Western Canada. In M. Woo (Ed.), *Cold region atmospheric and hydrologic studies. The Mackenzie GEWEX experience*, (pp. 81–96). Berlin, Heidelberg: Springer. https://doi.org/10.1007/978-3-540-75136-6_5

Pomeroy, J. W., Marks, D., Link, T., Ellis, C., Hardy, J., Rowlands, A., & Granger, R. (2009). The impact of coniferous forest temperature on incoming longwave radiation to melting snow. *Hydrological Processes*, *23*(17), 2513–2525. https://doi.org/10.1002/hyp.7325

Pulliainen, J., Aurela, M., Laurila, T., Aalto, T., Takala, M., Salminen, M., et al. (2017). Early snowmelt significantly enhances boreal springtime carbon uptake. *Proceedings of the National Academy of Sciences of the United States of America*, *114*(42), 11,081–11,086. https://doi.org/10.1073/pnas.1707889114

Qu, X., & Hall, A. (2014). On the persistent spread in snow-albedo feedback. *Climate Dynamics*, *42*(1–2), 69–81. https://doi.org/10.1007/s00382-013-1774-0

Reid, T. D., & Essery, R. L. H. (2013). New methods to quantify canopy structure of leafless boreal birch forest from hemispherical photographs. *Open Journal of Forestry*, *03*(2), 70–74. https://doi.org/10.4236/ojf.2013.32012

Román, M. O., Schaaf, C. B., Woodcock, C. E., Strahler, A. H., Yang, X., Braswell, R. H., et al. (2009). The MODIS (Collection V005) BRDF/albedo product: Assessment of spatial representativeness over forested landscapes. *Remote Sensing of Environment*, *113*(11), 2476–2498. https://doi.org/10.1016/j.rse.2009.07.009

Roth, T. R., & Nolin, A. W. (2017). Forest impacts on snow accumulation and ablation across an elevation gradient in a temperate montane environment. *Hydrology and Earth System Sciences*, *21*(11), 5427–5442. https://doi.org/10.5194/hess-21-5427-2017

Rutter, N., Essery, R., Pomeroy, J., Altimir, N., Andreadis, K., Baker, I., et al. (2009). Evaluation of forest snow processes models (SnowMIP2). *Journal of Geophysical Research*, 114, D06111. https://doi.org/10.1029/2008JD011063

Sailor, D. J., & Fan, H. (2002). Modeling the diurnal variability of effective albedo for cities. *Atmospheric Environment*, *36*(4), 713–725. https://doi.org/10.1016/S1352-2310(01)00452-6

Schaaf, C. B., Gao, F., Strahler, A. H., Lucht, W., Li, X., Tsang, T., et al. (2002). First operational BRDF, albedo nadir reflectance products from MODIS. *Remote Sensing of Environment*, *83*(1–2), 135–148. https://doi.org/10.1016/S0034-4257(02)00091-3

Seyednasrollah, B., & Kumar, M. (2014). Net radiation in a snow-covered discontinuous forest gap for a range of gap sizes and topographic configurations. *Journal of Geophysical Research: Atmospheres*, *119*, 10,323–10,342. https://doi.org/10.1002/2014JD021809

Sicart, J. E., Essery, R. L. H., Pomeroy, J. W., Hardy, J., Link, T., & Marks, D. (2004). A sensitivity study of daytime net radiation during snowmelt to forest canopy and atmospheric conditions. *Journal of Hydrometeorology*, *5*(5), 774–784. https://doi.org/10.1175/1525-7541(2004)005<0774:ASSODN>2.0.CO;2

Stähli, M., Jonas, T., & Gustafsson, D. (2009). The role of snow interception in winter-time radiation processes of a coniferous sub-alpine forest. *Hydrological Processes*, *23*(17), 2498–2512). https://doi.org/10.1002/hyp.7180

Sturm, M., McFadden, J. P., Liston, G. E., Stuart Chapin, F., Racine, C. H., & Holmgren, J. (2001). Snow-shrub interactions in Arctic Tundra: A hypothesis with climatic implications. *Journal of Climate*, *14*(3), 336–344. https://doi.org/10.1175/1520-0442(2001)014<0336:SSIIAT>2.0.CO;2

Vrugt, J. A., Bouten, W., Dekker, S. C., & Musters, P. A. D. (2002). Transpiration dynamics of an Austrian Pine stand and its forest floor: Identifying controlling conditions using artificial neural networks. *Advances in Water Resources*, *25*(3), 293–303. https://doi.org/10.1016/S0309-1708(01)00061-6

Wang, W., Liang, S., & Augustine, J. A. (2009). Estimating high spatial resolution clear-sky land surface upwelling longwave radiation from MODIS data. *IEEE Transactions on Geoscience and Remote Sensing*, *47*(5), 1559–1570. https://doi.org/10.1109/TGRS.2008.2005206

Wang, Z., Erb, A. M., Schaaf, C. B., Sun, Q., Liu, Y., Yang, Y., et al. (2016). Early spring post-fire snow albedo dynamics in high latitude boreal forests using Landsat-8 OLI data. *Remote Sensing of Environment*, *185*, 71–83. https://doi.org/10.1016/j.rse.2016.02.059

Webster, C., & Jonas, T. (2018). Influence of canopy shading and snow coverage on effective albedo in a snow-dominated evergreen needleleaf forest. *Remote Sensing of Environment*, *214*, 48–58. https://doi.org/10.1016/j.rse.2018.05.023

Webster, C., Rutter, N., Zahner, F., & Jonas, T. (2016a). Measurement of incoming radiation below forest canopies: A comparison of different radiometer configurations. *Journal of Hydrometeorology*, *17*(3), 853–864. https://doi.org/10.1175/JHM-D-15-0125.1

Webster, C., Rutter, N., Zahner, F., & Jonas, T. (2016b). Modeling subcanopy incoming longwave radiation to seasonal snow using air and tree trunk temperatures. *Journal of Geophysical Research: Atmospheres*, *121*, 1220–1235. https://doi.org/10.1002/2015JD024099

Weihs, P., Lenoble, J., Blumthaler, M., Martin, T., Seckmeyer, G., Philipona, R., et al. (2001). Modeling the effect of an inhomogeneous surface albedo on incident UV radiation in mountaineous terrain: Determination of an effective surface albedo. *Geophysical Research Letters*, *28*(16), 3111–3114. https://doi.org/10.1029/2001GL012986

Wild, M., Ohmura, A., Gilgen, H., Morcrette, J. J., & Slingo, A. (2001). Evaluation of downward longwave radiation in general circulation models. *Journal of Climate*, *14*(15), 3227–3239. https://doi.org/10.1175/1520-0442(2001)014<3227:EODLRI>2.0.CO;2

Winkler, R., Boon, S., Zimonick, B., & Baleshta, K. (2010). Assessing the effects of post-pine beetle forest litter on snow albedo. *Hydrological Processes*, *24*(6), 803–812. https://doi.org/10.1002/hyp.7648

Wiscombe, W., & Warren, S. (1980). A model for the spectral albedo of snow. I: Pure snow. *Journal of the Atmospheric Sciences*, *37*, 2712–2733. https://doi.org/10.1175/1520-0469(1980)037<2712:AMFTSA>2.0.CO;2

Wolter, P. T., Berkley, E. A., Peckham, S. D., Singh, A., & Townsend, P. A. (2012). Exploiting tree shadows on snow for estimating forest basal area using Landsat data. *Remote Sensing of Environment*, *121*, 69–79. https://doi.org/10.1016/j.rse.2012.01.008

Yuan, H., Dai, Y., Dickinson, R. E., Pinty, B., Shangguan, W., Zhang, S., et al. (2017). Reexamination and further development of two-stream canopy radiative transfer models for global land modeling. *Journal of Advances in Modeling Earth Systems*, *9*, 113–129. https://doi.org/10.1002/2016MS000773

Yuan, H., Dickinson, R. E., Dai, Y., Shaikh, M. J., Zhou, L., Shangguan, W., & Ji, D. (2014). A 3D canopy radiative transfer model for global climate modeling: Description, validation, and application. *Journal of Climate*, *27*(3), 1168–1192. https://doi.org/10.1175/JCLI-D-13-00155.1

Zhang, Y., Chen, J. M., & Miller, J. R. (2005). Determining digital hemispherical photograph exposure for leaf area index estimation. *Agricultural and Forest Meteorology*, *133*(1–4), 166–181. https://doi.org/10.1016/j.agrformet.2005.09.009